Resonance Couplings in Si@MoS$_2$ Core–Shell Architectures

Tatsuki Hinamoto, Yea-Shine Lee, Sina Abedini Dereshgi, Jennifer G. DiStefano, Roberto dos Reis, Hiroshi Sugimoto, Koray Aydin, Minoru Fujii,* and Vinayak P. Dravid*

Heterostructures of transition metal dichalcogenides and optical cavities that can couple to each other are rising candidates for advanced quantum optics and electronics. This is due to their enhanced light–matter interactions in the visible to near-infrared range. Core–shell structures are particularly valuable for their maximized interfacial area. Here, the chemical vapor deposition synthesis of Si@MoS$_2$ core–shells and extensive structural characterization are presented. Compared with traditional plasmonic cores, the silicon dielectric Mie resonator core offers low Ohmic losses and a wider spectrum of optical modes. The magnetic dipole (MD) mode of the silicon core efficiently couples with MoS$_2$ through its large tangential component at the core surface. Using transmission electron microscopy and correlative single-particle scattering spectroscopy, MD mode splitting is experimentally demonstrated in this unique Si@MoS$_2$ core–shell structure. This is evidence for resonance coupling, which is limited to theoretical proposals in this particular system. A coupling constant of 39 meV is achieved, which is ≈1.5-fold higher than previous reports of particle-on-film geometries with a smaller interfacial area. Finally, higher-order systems with the potential to tune properties are demonstrated through a dimer system of Si@MoS$_2$, forming the basis for emerging architectures for optoelectronic and nanophotonic applications.

1. Introduction

Heterostructures of 2D materials and optical cavities are powerful platforms that make them strong candidates for optics and electronics applications. Recently, transition metal dichalcogenides (TMDs) have been gathering much attention as a family of 2D semiconducting quantum emitters to construct such heterostructures. This is due to their strong binding energy and transition dipole moment of their excitons at room temperature.[1–3] A variety of cavities have been coupled with TMDs.[4,5]

By integrating such excitons into optical cavities, the excitonic properties can be flexibly manipulated to yield enhanced light–matter interactions. This has direct applications in optoelectronic devices such as light sources, lasers, single-photon sources, and chiral sensing devices.[3,4,6–14]

Because the optical manipulation of excitons in the heterostructures relies on the optical coupling between cavity resonances and excitons, demonstrating couplings with various coupling strengths is important to realize various state-of-the-art devices such as quantum information processing, all-optical switches, and exciton–polariton lasers.[3,4,6–14] For example, in the Fano resonance regime (weak coupling), the cavity resonance can enhance spontaneous emission of excitons by the Purcell effect.[14,15] Moreover, emission directionality and spectral shape can be engineered by Fano interference, which is useful in sensors, data storage technology, and topological optics.[16] In the mode splitting regime (strong coupling), the coherent energy exchange between the excitonic transition and the resonant cavity exceeds the rate of spontaneous decay. Consequently, hybrid states, so-called exciton–polaritons, are generated, enabling the modification of the nature of the cavity itself.[17]

Before further discussion, it is important to note that there is no conclusive definition of coupling strength in the field. Here, we adopt the terms used by Wang et al. in which the coupling strength is determined by comparing $2g$ to $(\gamma_m - \gamma_e)/2$, where g is the coupling constant and γ is the damping factor of the systems involved in resonance coupled oscillation.[18] However,

T. Hinamoto, H. Sugimoto, M. Fujii
Department of Electrical and Electronic Engineering
Graduate School of Engineering
Kobe University
Rokkodai Nada, Kobe 657–8501, Japan
E-mail: fujii@eedept.kobe-u.ac.jp
Y.-S. Lee, J. G. DiStefano, R. dos Reis, V. P. Dravid
Department of Materials Science and Engineering
Northwestern University
Evanston, IL 60208, USA
E-mail: v-dravid@northwestern.edu

S. A. Dereshgi, K. Aydin
Department of Electrical and Computer Engineering
Northwestern University
Evanston, IL 60208, USA
J. G. DiStefano, V. P. Dravid
International Institute for Nanotechnology (IIN)
Northwestern University
Evanston, IL 60208, USA
R. d. Reis, V. P. Dravid
Northwestern University Atomic and Nanoscale Characterization
Experimental (NUANCE) Center
Northwestern University
Evanston, IL 60208, USA

**ADVANCED
SCIENCE NEWS**
www.advancedsciencenews.com

NANO · MICRO

small

www.small-journal.com

other reports have defined the coupling strength based on dips in the absorption spectra,[19] or by comparing the scattering peak separation to the width of the modes.[20]

Plasmonic cavities have been most studied because of the compact mode volume (V), which increases g (e.g., $g \propto 1/\sqrt{V}$).[13,21–23] However, plasmonic cavities inherently possess Ohmic losses around the frequency of excitonic transitions. This limits not only their applications but also the coupling strength by dissipating energy from the system and altering the excitonic behavior.[13] Additionally, the incompatibility to the complementary metal-oxide-semiconductor (CMOS) processes restricts the utility of plasmonic metals in terms of fabrication.

Dielectric nanocavities empowered by Mie resonance offer a solution to these issues due to many advantages such as low loss nature and CMOS compatibility. Owing to the high refractive index (n) of conventional semiconductors such as silicon ($n \sim 4$), a dielectric nanocavity can strongly confine light and resonate in the visible and near-infrared range at match with exciton wavelengths of TMDs. Extensive studies have been reported recently on heterostructures of dielectric nanocavities and TMDs and have demonstrated emission directionality control,[3,24,25] manipulation of single photon emission,[26] enhanced nonlinear effects,[27] and so on.[28–30] Compared to their plasmonic counterparts, the dielectric nanocavities have a larger effective mode volume, which competes with increasing their coupling constant. Despite this, their possession of the magnetic dipole (MD) mode can be advantageous to achieve a high coupling constant because an MD induces a tangential electric field on the core surface. In addition to the maximized interfacial area in the core–shell geometry, this advantage enables an efficient interaction between the MD mode and the in-plane excitons of the encapsulating TMDs.

Core–shell heterostructures made of a spherical Mie resonator encapsulated by TMDs have been theoretically proposed by several groups as a fascinating candidate with one of the highest coupling constants.[18,31–33] This stems from the resonant coupling of the MD with TMD's excitonic transitions. For example, Lepeshov et al. theoretically reported that a core–shell heterostructure of a silicon nanosphere covered by monolayer WS$_2$ can have Rabi splitting energy of 110 meV (i.e., $g = 55$ meV), falling into the strong coupling regime.[31] Wang et al. also studied the core–shell heterostructure and numerically derived $g = 29$ meV, while reassessing the previous report on strong coupling.[18] Despite the attractive potential, however, the fabrication of such a core–shell structure is challenging. Therefore, both reports relied on a dispersion of silicon nanospheres on a monolayer tungsten disulfide (WS$_2$), so-called a particle-on-film geometry, resulting in degraded experimental coupling constants of $g = 24.5$ meV[31] and 12.5 meV,[18] respectively. Experimental results are yet to be reported on the resonance coupling of Mie resonators with TMDs in core–shell heterostructures. Moreover, the attractive high coupling constant that has been reported in silicon nanoparticles with organic dye molecules[34] is yet to be demonstrated with TMDs.

Here, we report a bottom-up synthesis of the core–shell heterostructure made of silicon nanospheres covered by multilayer-MoS$_2$. Because the silicon nanospheres are independent of the substrate, our fabrication protocol accommodates facile transfer of core–shells. This enables an experimental demonstration of mode splitting at the level of an individual core–shell particle. By nature of spherical geometry, the exciton orientation is well-defined as well, which facilitates robust theoretical analyses as the analytical solution of the optical response of such a geometry is well-known.

We first theoretically analyze the optical behavior of the heterostructure by Mie theory and the coupled mode theory (CMT). It shows that a theoretical coupling constant of $g = 50$ meV can be expected. We then grow thin MoS$_2$ layers around crystalline silicon nanospheres with diameters of 100–200 nm in a bottom-up manner using chemical vapor deposition (CVD). Detailed structural analysis by electron microscopy exhibits successful formation of continuous MoS$_2$ shells over the surface of the silicon core. We then measure the scattering spectra for the synthesized heterostructure and observe mode splitting of the MD peak in agreement with simulations. Fitting the experimental scattering spectrum by CMT, we achieve a coupling constant of $g = 39$ meV, which is ≈1.5 times higher than the value from the particle-on-film geometry in previous reports.[18,31] In contrast to previous heterostructures, our system is standalone (i.e., free from substrates) and thus advantageous for many applications. We also demonstrate a dimer system of the core–shell heterostructures to show the capability to construct higher-order structures such as multi-mers, which enrich the array of aforementioned potential applications.

2. Results and Discussion

2.1. Theoretical Analyses of the Optical Coupling in the Core–Shell Heterostructures

We start from a theoretical analysis of a core–shell heterostructure consisting of a silicon nanosphere encapsulated with a multilayer-MoS$_2$ shell. The calculation model is shown in **Figure 1**a. The structure consists of a silicon sphere with a radius a ($= R_{core}$) and a six-layer MoS$_2$ shell with an outer radius b. This shell thickness is chosen because it is within the range (≈5 to 15 layers) of our synthesis results and frequently observed. We assume each MoS$_2$ layer is 0.63 nm thick based on experimental lattice spacing measurements of MoS$_2$ shells, which is in agreement with literature values.[10] Slight deviations from reported values may arise due to the curvature of the core surface and resulting strain in the shell.

Given the recently reported giant optical anisotropy of TMDs between the crystallographic ab-plane and c-axis,[35] the permittivity of the shell should be treated as radially anisotropic, while the core is isotropic. The anisotropic optical response of bulk MoS$_2$ is taken from literature and is shown in the Supporting Information (Figure S1, Supporting Information). We assume the shell is uniformly grown around the core, and the normal and tangential components of the permittivity can be expressed as ε_c and ε_{ab} representing, respectively, the permittivity of MoS$_2$ corresponding to the ab-plane and the c-axis. The optical responses of a core–shell system with a radially anisotropic shell are theoretically derived as an extension of Mie theory[36] by Roth and Dignam.[37] Here, we developed a calculation program following the expression provided by Tang et al.[38] that gives a simpler prospect.
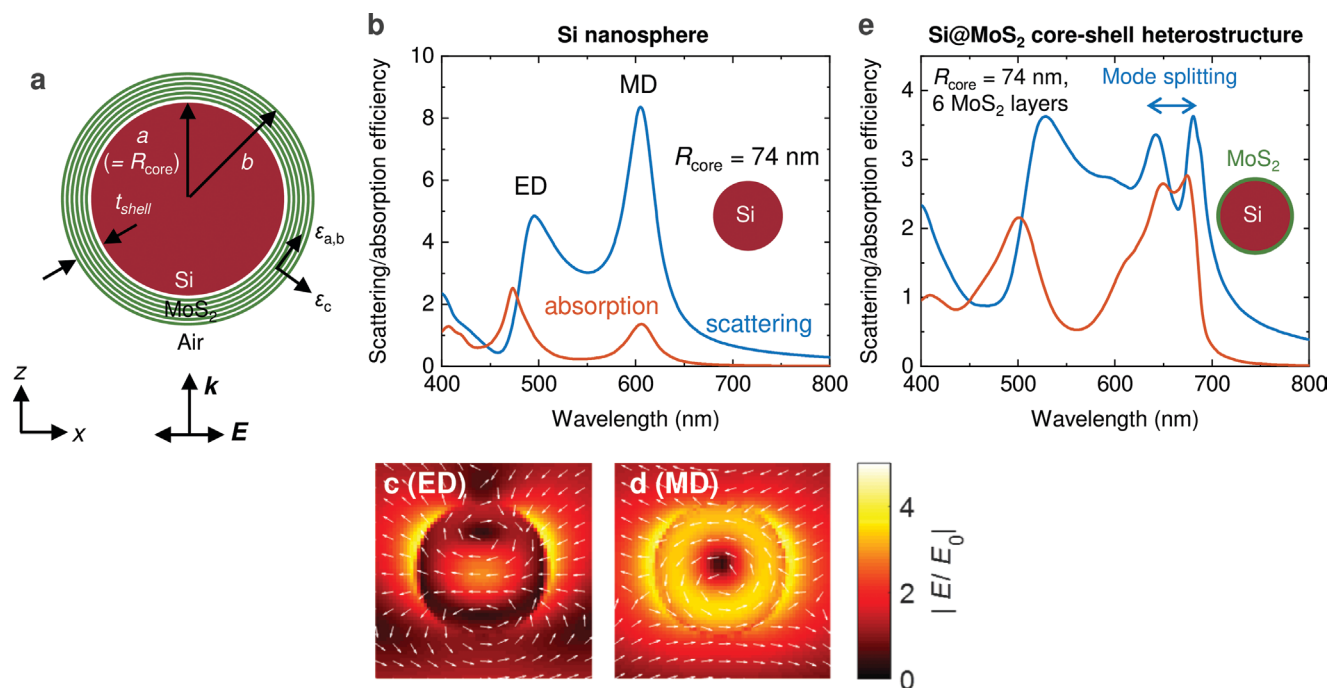
ADVANCED
SCIENCE NEWS
www.advancedsciencenews.com

NANO · MICRO
small
www.small-journal.com

Figure 1. Theoretical calculation of the scattering properties of the Si@MoS$_2$ core–shell heterostructure. a) Calculation model. b,e) Scattering (blue line) and absorption (orange line) spectra of b) silicon nanosphere and e) Si@MoS$_2$ core–shell heterostructure. c,d) Electric field distributions of electric dipole (ED; 496 nm) and magnetic dipole (MD; 602 nm) Mie resonances of the silicon nanosphere. The radius of the silicon nanosphere is 74 nm, and the MoS$_2$ shell thickness of the heterostructure is six layers.

Figure 1b shows the scattering and absorption spectra of a silicon sphere with radius $R_{core} = 74$ nm. Optical modes present in the spectra are the electric dipole (ED) and MD modes, caused by collective polarization and electrical displacement current loops, respectively. The silicon sphere exhibits typical scattering peaks of ED and MD modes of Mie resonance at 496 and 602 nm, respectively. The absorption spectrum also shows two peaks around 600 and 470 nm, which originate from MD and magnetic quadrupole modes. The field profiles at the ED and MD peak wavelengths are shown in Figure 1c,d in the xz-plane. The rotation of the electric field in the MD mode intuitively suggests more efficient coupling with the in-plane exciton of MoS$_2$ than the ED mode because of the higher tangential component at the surface.

We then analyze a Si@MoS$_2$ core–shell heterostructure with the same core radius. The scattering and absorption spectra of the heterostructure are shown in Figure 1e. As a reference, the spectra of the MoS$_2$ shell alone are also provided in Figure S12 in the Supporting Information. The formation of the shell slightly red-shifts the resonance wavelengths of ED and MD of the silicon sphere, and the MD spectrally matches with the MoS$_2$ intralayer A-exciton transition ≈665 nm. As can be seen, the interaction between the two resonances results in significant splitting of the MD scattering peak into upper and lower energy branches. Such a behavior has previously been discussed in a similar system, Si@monolayer-WS$_2$, and the mechanism was explained by the MD mode-mediated enhanced absorption originating from the energy transfer process. Although the system is similar, our system is composed of multilayer-MoS$_2$ and results in somewhat different spectral features. For example, the absorption peak of the MD also exhibits a small splitting at the exciton wavelength.

To quantitatively discuss the interaction in our core–shell system, we fit the scattering spectrum and extract the coupling constant using CMT with coupled Lorentz oscillators (see the Experimental Section).[39,40] The coupling constant determines the coupling regime of the system based on a well-known criterion: $2g > (\gamma_m - \gamma_e)/2$ for mode splitting (strong coupling) and $2g < (\gamma_m - \gamma_e)/2$ for Fano resonance (weak coupling), where γ_m and γ_e are the broadening factors of magnetic dipole and exciton resonances, respectively.[18,31,39]

The scattering spectrum of the core–shell heterostructure in Figure 1e is well fitted by the CMT (see Figure S2, Supporting Information). The coupling constant is calculated to be $g = 50$ meV, with broadening factors $\gamma_m = 110$ meV and $\gamma_e = 100$ meV. Hence, satisfaction of $2g > (\gamma_m - \gamma_e)/2$ as well as the small dip in the absorption spectrum satisfies the conditions for mode splitting regime. Note the obtained coupling constant ($g = 50$ meV) is comparable to the theoretical value for Si@monolayer-WS$_2$ core–shell system (55 meV[31] or 29 meV[18]). Considering that γ_e in our system is about two times larger than the reported value in the latter system, avenues for future research may entail exploring systems which can decrease the broadening factor of TMDs by chemical doping, strain engineering, or by replacing the surrounding environment to higher refractive index materials.

To gain further physical insights into the system, we provide a calculated core radius-dependent scattering spectrum in **Figure 2**. By changing the core radius of the core–shell system, the Mie resonance wavelengths are swept over the wavelength

**ADVANCED
SCIENCE NEWS**
www.advancedsciencenews.com

**NANO · MICRO
small**
www.small-journal.com

of the exciton transition to alter the degree of interaction of the two resonators. Figure 2a shows the 2D map of the scattering spectrum when the core radius is changed from 50 to 150 nm. The shell thickness is again fixed to six layers. The Mie resonance wavelengths of ED and MD can be tuned almost linearly over the entire visible range with increasing the radius. This is in agreement with a condition of Mie resonance, $2R \sim \lambda/n$, where R, λ, and n are core radius, wavelength, and refractive index, respectively, for the MD mode.[41] When the MD resonance wavelength spectrally intersects the exciton resonance (dashed line), anticrossing behavior can be seen. Note that the ED mode also exhibits similar behavior, but the peak splitting is not as obvious as the MD. This indicates the expected stronger interaction of MD with the exciton than ED.

Figure 2b is an enlarged view of the 2D map around the condition where the MD and exciton transition wavelengths overlap. The black lines show the fitted result of the spectrum by CMT, and the dashed lines indicate the spectral position that corresponds to the Mie MD and the exciton resonances. It can now be seen more clearly that the scattering peak of the MD splits into higher ($\omega+$) and lower energy branches ($\omega-$) at the position of the exciton resonance. This typical anticrossing behavior again confirms the occurrence of resonance coupling between

two resonators. Note that the structural parameter in Figure 1e, $R_{core} = 74$ nm, gives the largest coupling (i.e., $g = 50$ meV) in the range of Figure 2b. These theoretical results confirm the potential of the Si@MoS$_2$ core–shell heterostructure to achieve a high coupling strength in a dielectric nanoparticle and TMDs hybrid system.

2.2. Experimental Realization of Si@MoS$_2$ Core–Shell Heterostructures

In order to experimentally demonstrate coupling in the Si@MoS$_2$ core–shell heterostructure, we have developed a method to encapsulate silicon nanospheres with MoS$_2$ by a bottom-up process. The details of the fabrication method are provided in the Experimental Section. Briefly, crystalline silicon nanospheres are synthesized as a colloidal form and dispersed on a substrate.[42–44] MoS$_2$ layers then encapsulate the silicon nanospheres by CVD, and hundreds of core–shells can be fabricated at once on a single growth substrate.[45,46] Finally, the synthesized Si@MoS$_2$ core–shell heterostructures are isolated from the growth substrate into ethanol solution. It is important to note that silicon nanospheres range in diameter from 100 to 200 nm to sufficiently span the coupling range as presented in Figure 2. In addition, the shell thickness spans around 5 to 15 layers due to the nature of the CVD process and varying growth conditions on the substrate at the microscale. It is also possible to have defects in the form of truncated shell layers around a nanosphere.[46] However, the overall range in experimental shell thicknesses is narrow enough to be considered homogenous for our purposes, and even beneficial to accommodate the size range in silicon nanospheres and experimentally identify the best coupling core–shell parameters.

Transmission electron microscopy (TEM) and scanning TEM (STEM) techniques, such as energy dispersive X-ray spectroscopy (EDS) are used to conduct structural and chemical characterizations of the synthesized nanoparticles. Annular dark-field (ADF)-STEM in **Figure 3**a shows a collection of multiple successfully encapsulated nanoparticles, ensuring consistency of the synthesis process. The encapsulation is effective regardless of the nanoparticle size (more examples are shown in Figure S3, Supporting Information). A complete and conformal MoS$_2$ encapsulation is observed in most of the silicon nanoparticles, and a representative example is shown in Figure 3b. MoS$_2$ shells are depicted in the ADF-STEM image by a brighter contrast due to the higher atomic number of molybdenum (Mo Z = 42) in comparison to the silicon (Si Z = 14) core. High-resolution ADF image in Figure 3c shows the edge of Si@MoS$_2$ with five MoS$_2$ layers spaced by 0.63 nm. Localized defects such as an incomplete external shell[46] can be visualized. These discontinuities are often seen in core–shell morphologies and can offer further opportunities for tuning the core–shell structure interaction with its environment, since TMD edges contain reactive dangling bonds.[46,47]

Raman spectroscopy validates the core–shell structure observed in the TEM (Figure S3, Supporting Information). The A$_{1g}$ and E$^1_{2g}$ phonon modes of MoS$_2$ shell layers are detected near 401 and 382 cm^{-1}, respectively,[48] reflecting values reported in literature. EDS is employed to identify the
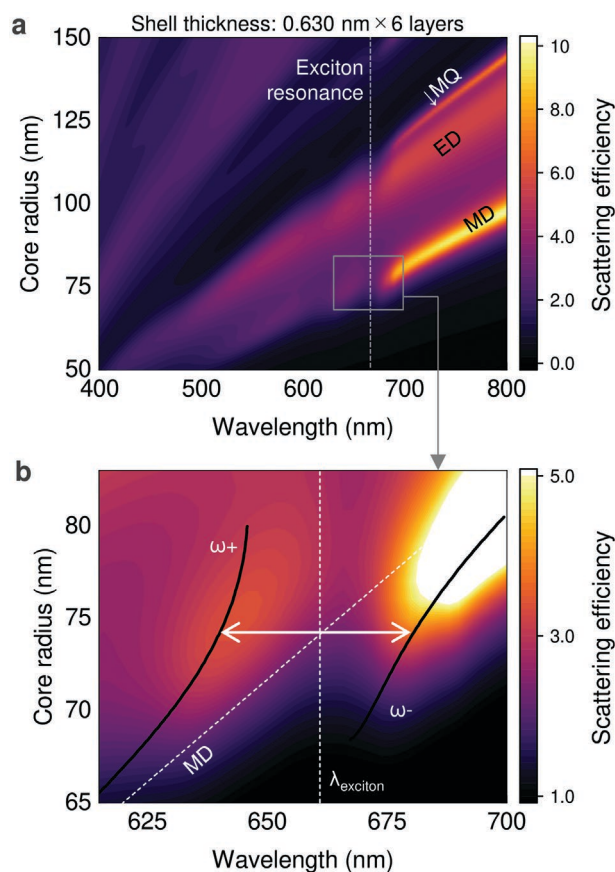

Figure 2. Analysis of the resonance coupling in the Si@MoS$_2$ core–shell system for different silicon core radii. a) Scattering efficiency map as a function of wavelength and core radius. b) Enlarged view of the map around the intersection of MD and excitonic resonances. The black lines indicate fitted results by CMT.
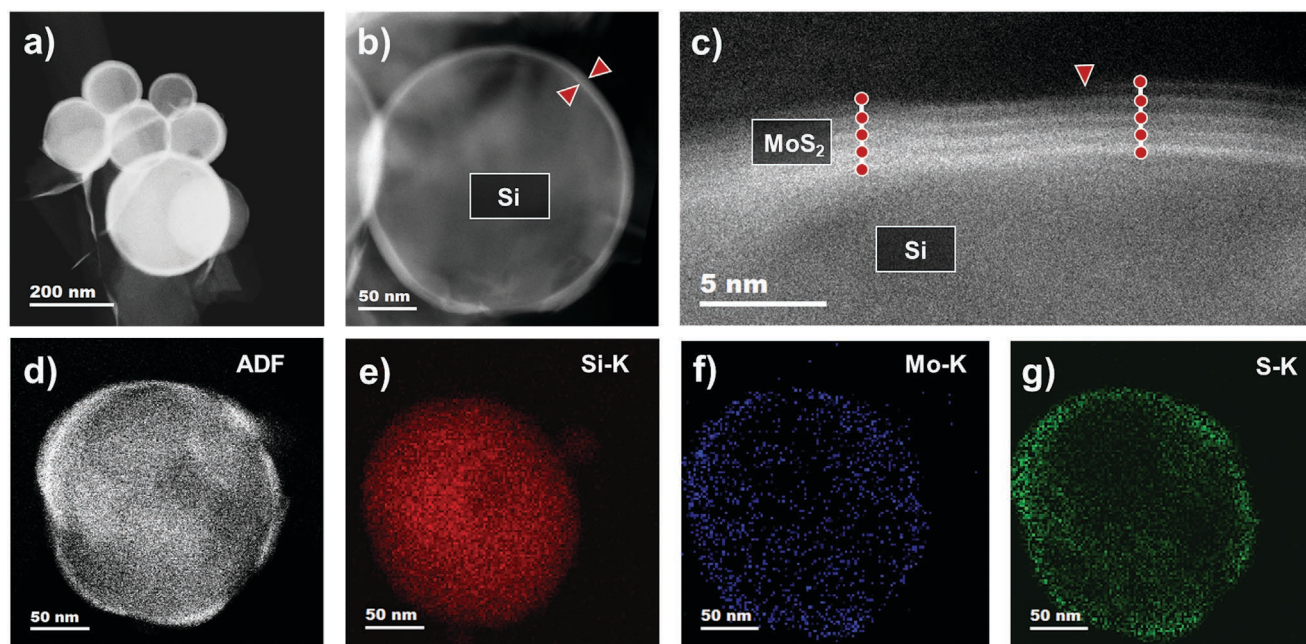
Figure 3. Structural and chemical analysis of an MoS$_2$ encapsulated silicon nanoparticle. a) ADF-STEM image of an ensemble of Si@MoS$_2$ nanoparticles. b) A magnified ADF-STEM image of a Si@MoS$_2$ emphasizing the conformal encapsulation pointed by red arrows. c) High-resolution ADF-STEM depicting the MoS$_2$ shells in detail. The red dots mark each one of the MoS$_2$ layers with interlayer spacing of 0.63 nm and the red arrow points to an incomplete MoS$_2$ shell. d) ADF-STEM image of a Si@MoS$_2$ with (e)–(g) showing the simultaneously acquired elemental maps for silicon, molybdenum, and sulfur via STEM-EDS.

chemical composition of the core–shell architecture. The silicon (Si), molybdenum (Mo), and sulfur (S) K-peaks at 1.74, 17.48, and 2.31 keV, respectively, are used to generate a chemical map as shown in Figure 3e–g accompanied by simultaneously acquired ADF-STEM. Si signal is heavily detected at the core, while the Mo and S signals are detected at both the core and the edge. Although the S-K line partially overlaps the Mo-L line at 2.29 keV (Figure S4, Supporting Information), the Mo and S signals result from the same area in the structure. Therefore, this overlap does not affect the determination of chemical element distribution. Moreover, the brighter signal of Mo and S at the edge is due to the absence of intervening silicon signal at the shell of the structure.

We then present dark-field single particle scattering spectra of the Si@MoS$_2$ core–shell heterostructures to experimentally demonstrate the resonance coupling. As shown in **Figure 4**a, the optical measurement is conducted on a free-standing 10 nm thick silicon nitride membrane as a substrate. The optically thin substrate allows us to ignore substrate-induced effects and to treat nanoparticles as being suspended in free-space.[49] In addition, this enables rigid characterization of optical properties of the nanoparticles, which have some variation in core radii, by tracking exactly the same nanoparticle under TEM and optical microscope. The measurement geometry of the scattering spectrum is shown in Figure 4b. The sample is placed face-down on a custom-built inverted microscope and shone by white light from the bottom in a dark-field mode via an objective (100×). The scattered light from each particle is collected by the objective and relayed to a spectrometer. Note that the measurable angular range is limited by the numerical aperture (N.A. = 0.9) of the objective, that is 128°.

The measured scattering spectra of three Si@MoS$_2$ core–shell heterostructures are shown in Figure 4c–e (red line). Raman signals of each particle are shown together on the top panels (black line) to confirm the components. The corresponding TEM images are shown in Figure 4f–h, respectively. Additionally, more scattering spectra of different sized particles are provided in Figure S10 in the Supporting Information. Before discussing the results for the heterostructure, it is worth noting that our silicon nanospheres exhibit scattering spectra that agree almost perfectly with simulations as shown in Figure S5 in the Supporting Information.[49,50]

Beginning with the smallest particle, Figure 4c shows the scattering spectrum of a particle whose core diameter (D_{Si}) estimated from Figure 4f is 111 nm. The scattering peak of the MD resonance is seen around 500 nm, while the ED resonance appears as a shoulder on the short wavelength side of the MD peak. In such a range, the Mie resonance is spectrally apart from the exciton transition wavelength (≈670 nm). Thus, no specific feature attributed to the encapsulation is observed, though the formation of the MoS$_2$ shell is confirmed by the Raman spectrum and TEM image.

In Figure 4d, the scattering spectrum of a larger particle (D_{Si} ~143 nm) is presented. The representative MoS$_2$ shell thickness is estimated to be ≈8 nm (Figure 4g). The Mie resonance wavelengths are larger, and the MD and the excitonic resonances now coincide at 670 nm. As expected by theoretical simulation (Figure 2), a clear splitting of the MD peak is observed. The width of the split reaches 50 nm. The measured spectral feature is qualitatively reproduced in the simulated scattering efficiency spectrum shown by the blue dashed line (reproduced in Figure S6, Supporting Information), which
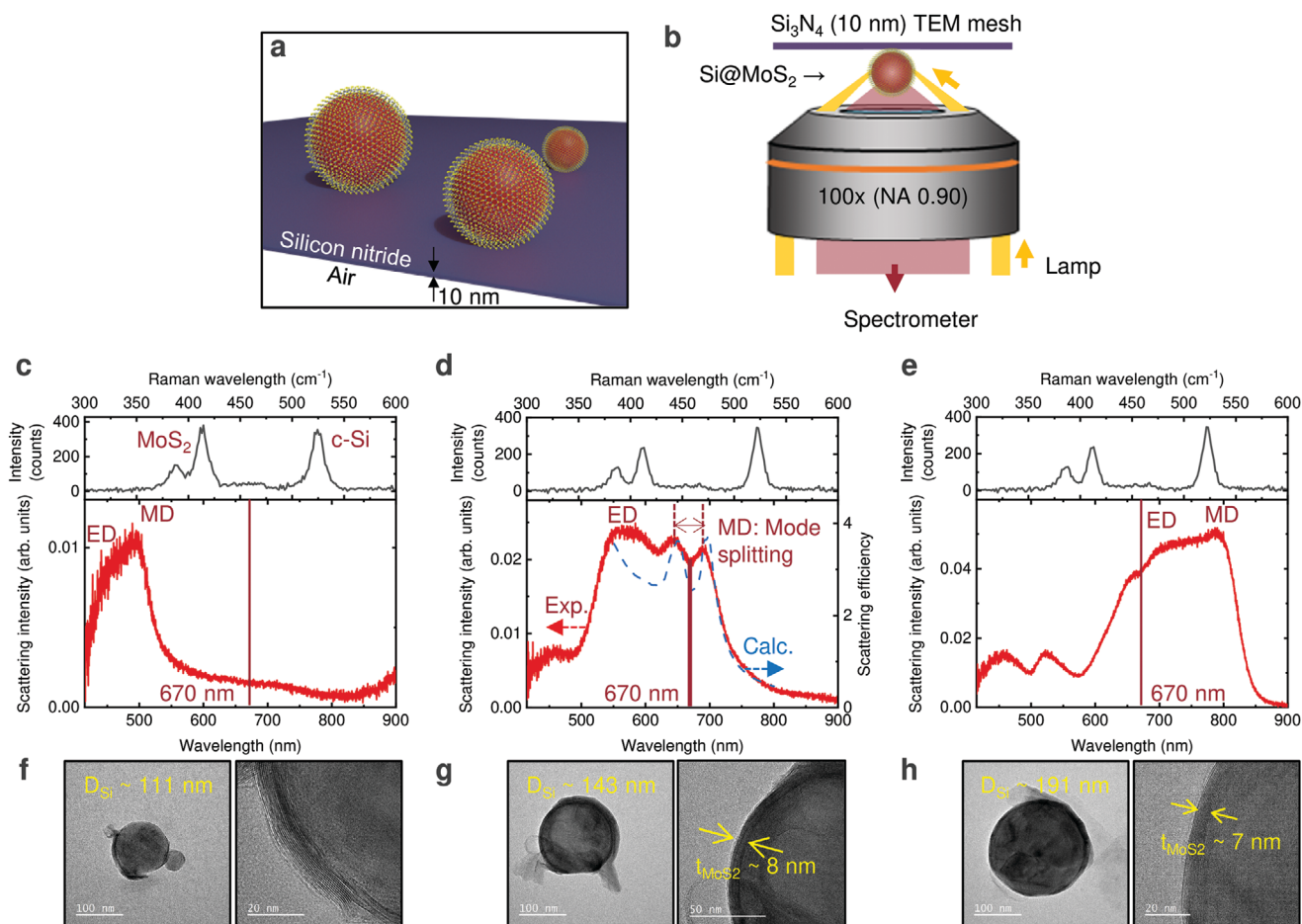
**ADVANCED
SCIENCE NEWS**
www.advancedsciencenews.com

NANO · MICRO
small
www.small-journal.com

Figure 4. Experimentally measured scattering spectra of individual Si@MoS$_2$ core–shell heterostructures. a,b) Schematic illustrations of a) experimental configuration where the heterostructures are placed on a 10 nm thick silicon nitride membrane and b) dark-field single particle spectroscopy. c–e) Scattering spectra (bottom) and Raman signals (top) of individual heterostructures with different sizes. Blue dashed line in (d) is the calculated scattering spectra based on CMT. f–h) TEM images (left) and magnified areas (right) of the particles corresponding to (c)–(e).

further supports the successful demonstration of the resonance coupling in the Si@MoS$_2$ core–shell heterostructure.

For the largest particle (D_{Si} ~191 nm) in Figure 4e,h, the MD resonance wavelength is even larger, and the wavelength of the ED resonance matches with that of the excitonic transition instead. Although a shallow dip is observed in the measured spectrum ≈670 nm, no significant peak splitting is noticed. This underscores the theoretical analysis that the excitonic resonance of MoS$_2$ can interact much more strongly with the MD resonance than the ED one in the core–shell system due to the orientation of the electric fields.

To quantitatively discuss the achieved coupling strength in our experiment, we extract a coupling constant by fitting the measured scattering spectrum in Figure 4d with CMT, similar to calculations in Figure 1. The obtained experimental coupling constant g reaches 39 meV with damping factors γ_m = 250 meV and γ_e = 110 meV (Figure S6 and Table S2, Supporting Information). This is close to the theoretical coupling constant of 50 meV (Figure S2 and Table S1, Supporting Information). The deviation between theory and experiment can be possibly attributed to the limited measurable angular range in the dark-field optical configuration and natural defects in shell formation.

The fact that the PL spectrum of the heterostructure exhibits a single peak (Figure S7, Supporting Information) is consistent with the CMT analysis. Mode splitting and single peaked PL spectrum reveal the mechanism of the observed peak split as Fano-type interference, or weak coupling. Nonetheless, the coupling strength in the proposed core–shell heterostructure is ≈1.5 to 2 times higher than previous reports of the particle-on-film geometry, c.f., g = 24.8[31] and 17.5.[18] It is also the highest among systems composed of an individual silicon Mie resonator and TMD (see Table S3, Supporting Information).

In addition to its potential to achieve a high coupling constant, the core–shell heterostructure is advantageous in its freedom to constitute more sophisticated systems and further control coupling strength. For example, the individual core–shell heterostructure can be elevated to multi-mers because it is independent from substrates. To this end, we then demonstrate a dimer system made of two core–shell heterostructures. **Figure 5**a shows the simulated scattering spectrum of a dimer composed of bare silicon nanospheres whose diameters are 153 nm. The dimer is illuminated by a plane-wave polarized along the dimer axis (i.e., axial polarization). The strongest peak around 610 nm (▼) can be assigned to a hybrid MD mode

where MD resonances of individual particles are hybridized.[51] The broad shoulder peak in the shorter wavelength range (≈520 nm) is dominated by the hybrid ED mode. Here again, we focus on the hybrid MD mode, and the electric and magnetic field profiles of the mode are shown in Figure 5b. The nature of the MD is still preserved in both particles, while an electric field that is three times greater than that of the monomer (Figure 1c) is induced in the gap between the particles. When the silicon nanospheres are encapsulated by MoS$_2$ shells, similar to the monomer case, the MD peak redshifts and splits at the wavelength of the exciton transition as shown in Figure 5c.

As silicon nanoparticles are randomly dispersed on the growth substrate prior to encapsulation, a Si@MoS$_2$ dimer system can also be formed during synthesis. Figure 5d shows the experimentally measured scattering spectrum of a dimer. The TEM image of the measured dimer is presented in Figure 5e, showing two core–shell heterostructures with core diameters of 120 and 112 nm. Although the sizes of the cores are slightly different, their MD resonances are spectrally close enough to form the hybrid mode. Indeed, the entire scattering spectrum shows a different behavior from the individual core–shell heterostructures in Figure 4 and is much broader. Comparing the measured spectrum with the simulated one, a reasonable agreement is seen. We can assign the peak around 600 nm to the hybrid ED mode and 650 and 700 nm ones to the split hybrid MD peaks. The additional peak around the 520 nm can be assigned to the ED mode that arises from the different polarization component (i.e., transverse polarization) (see Figure S11, Supporting Information). Importantly, the measured spectrum reproduces the splitting of the hybrid MD mode at the MoS$_2$ exciton wavelength (≈670 nm), offering evidence

of successful resonance coupling of the cores and shells in the dimer system.

We also apply the CMT to the experimental dimer system and extract the coupling constant. A coupling constant $g = 43.5$ meV is obtained with $\gamma_m = 320$ meV and $\gamma_e = 110$ meV. Although a slightly higher coupling constant than the monomer case is obtained, $2g = 87$ meV and $(\gamma_m - \gamma_e)/2 = 105$ meV indicate that the coupling falls within the Fano resonance regime (weak coupling, $2g < (\gamma_m - \gamma_e)/2$) because the large broadening factor, γ_m, increases the right side of the equation. Therefore, despite having a higher coupling constant ($g = 43.5$ meV), the hybrid MD mode in the dimer configuration shows weaker coupling than the MD mode in the monomer structure ($g = 39$ meV). Regardless, the capability to arrange core–shell systems into higher-order architectures in this way highlights the potential to tune known core–shell properties and introduce novel properties.

3. Summary and Conclusion

We reported a CVD method of synthesizing unique Si@MoS$_2$ core–shell heterostructures with silicon core diameters ranging from 100 to 200 nm, and shell thicknesses ranging from 5 to 15 layers. Raman signatures indicated the presence of MoS$_2$, and TEM and EDS results indicated correct chemical distribution in the structure. In addition, we achieved successful resonance coupling between the core and the shell in this system. This experimentally verifies previous theoretical reports in the field, and underscores the potential of a dielectric Mie resonator core to couple to TMDs for improved light-matter interaction in the core–shell system. Upon measuring the scattering spectra of various core–shells of different sizes, we observed the maximal resonance coupling in the Si@MoS$_2$ system of core diameter ≈143 nm and shell thickness ≈8 nm. The experimental coupling constant was measured ($g = 39$ meV) and revealed to be ≈1.5 times greater than those of previous reports on Si/TMD particle-on-film geometries. Our experimental coupling constant is in reasonable agreement with our theoretical one (50 meV) based on Mie theory and CMT. Not only is our system standalone with maximized interfacial area for improved coupling, but also we address the question of the coupling strength by quantifying the experimental mode splitting. This offers further advantages for practical core–shell applications in high-efficiency nanophotonic, optical, and electronic devices. Using dimers, we also showcase the versatility of core–shell structures and pave the way for engineering the Si@MoS$_2$ systems into more complex systems with tunability.

4. Experimental Section

Theoretical Calculation: *Coupled oscillator modeling*: Two interacting resonances could be modeled using coupled Lorentz oscillators in time domain as follows[39,40]

$$\ddot{x}_m(t) + \gamma_m \dot{x}_m(t) + \omega_m^2 x_m(t) + 2g\dot{x}_e(t) = F_m(t) \qquad (1)$$

where x_m represents the amplitude and phase of the mth oscillator (MD mode here), γ_m and ω_m are, respectively, the broadening factor
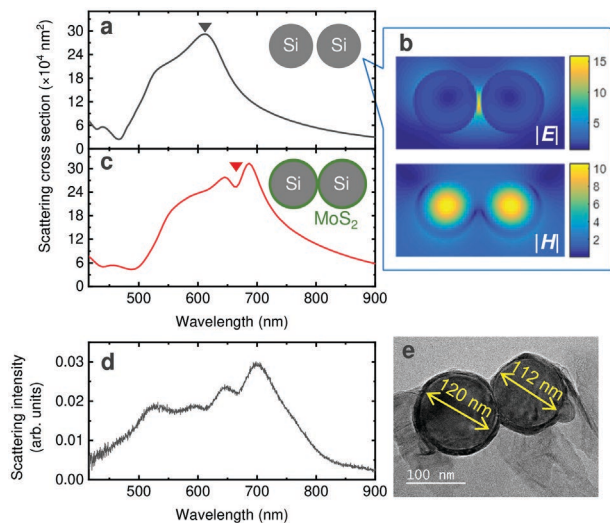

Figure 5. Resonance coupling of optical and exciton resonances in the dimer of the Si@MoS$_2$ core–shell system. a,c) Simulated scattering spectra of the dimer system consisting of a) bare silicon cores and c) Si@MoS$_2$ core–shell heterostructures. The diameter of both silicon cores is 153 nm, and the shell is six layers thick. The MD is marked with ▼. b) Simulated electric and magnetic field distributions of the bare dimer at the wavelength marked with ▼ in (a). d) Measured scattering spectrum and e) TEM image of the core–shell dimer.

ADVANCED
SCIENCE NEWS
www.advancedsciencenews.com

NANO · MICRO
small
www.small-journal.com

and resonance frequency, g and F_m, respectively, represents the coupling strength between oscillators m and e and driving force in the oscillator configuration. x_e is the amplitude of the other oscillator coupled to the oscillator m. The overdots in Equation (1) represent time derivatives. Since the driving force was electromagnetic, the driving force term had an oscillatory form of $F(t) = R(Fe^{-j\omega t}) = F\cos(j\omega t)$. Hence, the solutions had similar form of $x(t) = R(X(\omega)e^{-j\omega t})$. In order to model the system with the least fitting parameters, each peak (exciton and MD mode) was first isolated (uncoupled case) assuming $g = 0$ and solved in Fourier domain. The solution $X(\omega)$ could be linked to the scattering cross-section through $C_{scat}(\omega) \propto \omega^4 |F_m X_m(\omega)|^2$, which gives γ and ω_0 for exciton and MD modes as fitting parameters, along with F for amplitude. Afterward, the two coupled equations with $g \neq 0$ (in this case, coupled exciton and MD modes) could be solved in steady state in Fourier domain[52]

$$X_m(\omega) = \frac{(\omega^2 - \omega_e^2 + j\omega\gamma_e)F}{(\omega^2 - \omega_m^2 + j\omega\gamma_m)(\omega^2 - \omega_e^2 + j\omega\gamma_e) - 4\omega^2 g^2} \quad (2)$$

Setting F and g as the fitting parameters, C_{scat} is fitted, and g is obtained for simulation and experimental results.[18] All of the CMT equations were modeled in energy units of eV and meV. In order to transfer simulated and measured equations from wavelength to energy units, Jacobian conversion was applied.[53]

Finite-difference time-domain (FDTD) simulation: Simulations of the dimer system and all field profiles were conducted using the FDTD method (FDTD Solutions; Lumerical/Ansys). The dimer system was modeled in the same manner as theoretical calculation by Mie theory for the monomer, and the same material dispersion data were adopted for silicon[54] and MoS_2.[2] The radial anisotropy of MoS_2 was taken into account by specifying spatially varying orientation vectors using the built-in function "Liquid crystal rotation grid." Total-field scattered-field (TFSF) source was used to inject planewave. The scattering spectra were simulated as scattering cross-section by integrating all the scattered power in the scattered field region. Throughout this work, the existence of substrates was not considered, i.e., the particles were embedded in air.

Synthesis of Silicon Nanospheres: The silicon nanospheres were prepared by disproportionation of SiO at a high temperature.[42–44] Briefly, the SiO lumps (99.9%, Wako) were crushed and annealed at 1450 °C for 30 min in a N_2 gas atmosphere. This was resulted in a phase separation of SiO into Si and SiO_2 and growth of crystalline silicon nanospheres in a SiO_2 matrix. Nanospheres were extracted by dissolving the matrix using hydrofluoric acid.

Encapsulation of Silicon Nanospheres with MoS_2: *Chemical reagents*: The following reagents are used for the synthesis of MoS_2 shell layers: molybdenum (VI) oxide powder (99.5%, Sigma-Aldrich), and sulfur pieces (99.999%, Alfa Aesar). The growth substrate used was 525 µm thick (1-0-0) prime silicon wafer that was single-side polished with 300 nm of wet thermal oxide.

Synthesis: The stock solution of silicon nanoparticles was diluted in ethanol at 1:10 stock:ethanol ratio. Then, the diluted solution was drop casted on Si/SiO₂ growth substrates that were cut into ≈1 cm x 1 cm sizes. On this substrate, two drops of 2 µL perylene-3,4,9,10-tetracarboxylic acid tetrapotassium salt (PTAS) were dropped to promote MoS_2 growth. The synthesis process used was CVD in a tube furnace. Mini-Mite 1100 °C Single Zone Tube Furnace from Lindberg/Blue was used with a 22 mm ID x 25 mm OD 24 in. long fused quartz tube. Precursors of 350 mg of sulfur and 10 mg of molybdenum trioxide were placed in two separate alumina boats. The growth substrate with silicon nanoparticles drop casted was placed face down on the molybdenum trioxide boat such that the wafer sat balanced on the rim of the boat, bridged by two plain Si/SiO₂ wafers as depicted in Figure S8 in the Supporting Information.

The boat with sulfur was then placed a few centimeters from the edge of the furnace with a magnet behind it, while the boat with molybdenum trioxide was placed at the center of the heating zone (Figure S8, Supporting Information). The purpose of leaving the sulfur boat outside the furnace was to match the vaporization timing of sulfur with that of molybdenum trioxide during the reaction. Argon gas was used to purge the tube at 100 sccm for 15 min before implementing the heating profile at argon flow rate of 13 sccm. Starting from room temperature, the furnace was ramped to 700 °C in 40 min, held at 700 °C for 3 min of growth time before a natural cool down. When the center of the furnace reached 525 °C, a magnet was used to introduce the boat with sulfur into the edge of the furnace, where the temperature reached ≈150 °C during the growth time.

Structural Characterization: *TEM and STEM*: TEM samples were prepared by first bath sonicating the growth substrate for 10 min in a vial with ethanol solution. Then the sonicated solution was drop casted onto lacey carbon-coated copper TEM grids and left to dry. STEM images were obtained using Cs-corrected JEOL ARM200CF (JEOL Ltd.) operated at 200 kV. Convergence semiangle was set to 27.1 mrad using 40 µm condenser aperture, and the collection semiangles for ADF and annular bright-field were 90–370 and 10–23 mrad, respectively, using a probe current of about 70 pA. EDS signal was collected using two SDD detectors. EDS data collection was performed using Gatan Microscopy Suite (GMS) with STEM probe raster synchronized using Gatan Digiscan. TEM images and selected area electron diffraction patterns were obtained using a JEOL ARM300F (JEOL, Ltd.) operated at 300 kV.

Optical Measurement: A schematic of the optical measurement system is shown in Figure S9 in the Supporting Information. A custom-built inverted microscope was used for the scattering measurement. The individual nanospheres which were observed in the TEM were shone by white light from a halogen lamp in the dark-field epi-illumination mode. The scattered light was collected by a 100x objective and transferred to a spectrometer. Note that the detectable angular range was defined by the numerical aperture (NA = 0.90). The measurement system was also equipped with a CW Ar⁺ ion laser, allowing measurements of Raman and PL signals of exactly the same particle. The wavelength of the laser was 488 nm.

Supporting Information

Supporting Information is available from the Wiley Online Library or from the author.

Acknowledgements

Conflict of Interest

The authors declare no conflict of interest.

Author Contributions

T.H. and Y.-S.L. contributed equally to this work. The manuscript was written through contributions of all authors. All authors have given approval to the final version of the manuscript.

Data Availability Statement

The data that support the findings of this study are available from the corresponding author upon reasonable request.

Keywords

Mie resonance, radial anisotropy, resonant coupling, silicon nanospheres, transition metal dichalcogenides

[1] A. Chernikov, T. C. Berkelbach, H. M. Hill, A. Rigosi, Y. Li, O. B. Aslan, D. R. Reichman, M. S. Hybertsen, T. F. Heinz, *Phys. Rev. Lett.* **2014**, *113*, 076802.

[2] G. A. Ermolaev, Y. V. Stebunov, A. A. Vyshnevyy, D. E. Tatarkin, D. I. Yakubovsky, S. M. Novikov, D. G. Baranov, T. Shegai, A. Y. Nikitin, A. V. Arsenin, V. S. B. Volkov, *npj 2D Mater. Appl.* **2020**, *4*, 21.

[3] A. F. Cihan, A. G. Curto, S. Raza, P. G. Kik, M. L. Brongersma, *Nat. Photonics* **2018**, *12*, 284.

[4] Y. Ye, Z. J. Wong, X. Lu, X. Ni, H. Zhu, X. Chen, Y. Wang, X. Zhang, *Nat. Photonics* **2015**, *9*, 733.

[5] H. H. Fang, B. Han, C. Robert, M. A. Semina, D. Lagarde, E. Courtade, T. Taniguchi, K. Watanabe, T. Amand, B. Urbaszek, M. M. Glazov, X. Marie, *Phys. Rev. Lett.* **2019**, *123*, 067401.

[6] X. Fu, X. Fu, Y. Chen, L. Qin, H. Peng, R. Shi, F. Li, Q. Zhou, Y. Wang, Y. Zhou, Y. Ning, *J. Phys. Chem. Lett.* **2020**, *11*, 541.

[7] T. Chervy, S. Azzini, E. Lorchat, S. Wang, Y. Gorodetski, J. A. Hutchison, S. Berciaud, T. W. Ebbesen, C. Genet, *ACS Photonics* **2018**, *5*, 1281.

[8] L. Sortino, P. G. Zotev, S. Mignuzzi, J. Cambiaso, D. Schmidt, A. Genco, M. Aßmann, M. Bayer, S. A. Maier, R. Sapienza, A. I. Tartakovskii, *Nat. Commun.* **2019**, *10*, 5119.

[9] K. F. Mak, J. Shan, *Nat. Photonics* **2016**, *10*, 216.

[10] L. Sun, C.-Y. Wang, A. Krasnok, J. Choi, J. Shi, J. S. Gomez-Diaz, A. Zepeda, S. Gwo, C.-K. Shih, A. Alù, X. Li, *Nat. Photonics* **2019**, *13*, 180.

[11] J. Yan, Z. Zheng, Z. Lou, J. Li, B. Mao, B. Li, *Nanoscale Horiz.* **2020**, *5*, 1368.

[12] L. Britnell, R. M. Ribeiro, A. Eckmann, R. Jalil, B. D. Belle, A. Mishchenko, Y.-J. Kim, R. V. Gorbachev, T. Georgiou, S. V. Morozov, A. N. Grigorenko, A. K. Geim, C. Casiraghi, A. H. Castro Neto, K. S. Novoselov, *Science* **2013**, *340*, 1311.

[13] J. Sun, Y. Li, H. Hu, W. Chen, D. Zheng, S. Zhang, H. Xu, *Nanoscale* **2021**, *13*, 4408.

[14] E. M. Purcell, in *Confined Electrons and Photons: New Physics and Applications* (Eds: E. Burstein, C. Weisbuch), NATO ASI Series, Springer US, Boston, MA **1995**, pp. 839–839.

[15] M. Pelton, *Nat. Photonics* **2015**, *9*, 427.

[16] M. F. Limonov, M. V. Rybin, A. N. Poddubny, Y. S. Kivshar, *Nat. Photonics* **2017**, *11*, 543.

[17] J. T. Hugall, A. Singh, N. F. van Hulst, *ACS Photonics* **2018**, *5*, 43.

[18] H. Wang, J. Wen, W. Wang, N. Xu, P. Liu, J. Yan, H. Chen, S. Deng, *ACS Nano* **2019**, *13*, 1739.

[19] T. J. Antosiewicz, S. P. Apell, T. Shegai, *ACS Photonics* **2014**, *1*, 454.

[20] P. Törmä, W. L. Barnes, *Rep. Prog. Phys.* **2014**, *78*, 013901.

[21] M.-E. Kleemann, R. Chikkaraddy, E. M. Alexeev, D. Kos, C. Carnegie, W. Deacon, A. C. de Pury, C. Große, B. de Nijs, J. Mertens, A. I. Tartakovskii, J. J. Baumberg, *Nat. Commun.* **2017**, *8*, 1296.

[22] G. M. Akselrod, T. Ming, C. Argyropoulos, T. B. Hoang, Y. Lin, X. Ling, D. R. Smith, J. Kong, M. H. Mikkelsen, *Nano Lett.* **2015**, *15*, 3578.

[23] S. Wang, S. Li, T. Chervy, A. Shalabney, S. Azzini, E. Orgiu, J. A. Hutchison, C. Genet, P. Samorì, T. W. Ebbesen, *Nano Lett.* **2016**, *16*, 4368.

[24] T. Bucher, A. Vaskin, R. Mupparapu, F. J. F. Löchner, A. George, K. E. Chong, S. Fasold, C. Neumann, D.-Y. Choi, F. Eilenberger, F. Setzpfandt, Y. S. Kivshar, T. Pertsch, A. Turchanin, *ACS Photonics* **2019**, *6*, 1002.

[25] J. Yan, P. Yu, C. Ma, Y. Huang, G. Yang, *Nanotechnology* **2020**, *31*, 385201.

[26] L. Sortino, P. G. Zotev, C. L. Phillips, A. J. Brash, J. Cambiaso, E. Marensi, A. M. Fox, S. A. Maier, R. Sapienza, A. I. Tartakovskii, *Nat. Commun.* **2021**, *12*, 6063.

[27] N. Bernhardt, K. Koshelev, S. J. U. White, K. W. C. Meng, J. E. Fröch, S. Kim, T. T. Tran, D.-Y. Choi, Y. Kivshar, A. S. Solntsev, *Nano Lett.* **2020**, *20*, 5309.

[28] F. Xia, H. Wang, D. Xiao, M. Dubey, A. Ramasubramaniam, *Nat. Photonics* **2014**, *8*, 899.

[29] R. Mupparapu, T. Bucher, I. Staude, *Adv. Phys.: X* **2020**, *5*, 1734083.

[30] J. Yan, X. Liu, B. Mao, G. Yang, B. Li, *Adv. Opt. Mater.* **2021**, *9*, 2001954.

[31] S. Lepeshov, M. Wang, A. Krasnok, O. Kotov, T. Zhang, H. Liu, T. Jiang, B. Korgel, M. Terrones, Y. Zheng, A. Alú, *ACS Appl. Mater. Interfaces* **2018**, *10*, 16690.

[32] C. Tserkezis, P. A. D. Gonçalves, C. Wolff, F. Todisco, K. Busch, N. A. Mortensen, *Phys. Rev. B* **2018**, *98*, 155439.

[33] S. Lepeshov, A. Krasnok, A. Alù, *Nanotechnology* **2019**, *30*, 254004.

[34] G. W. Castellanos, S. Murai, T. V. Raziman, S. Wang, M. Ramezani, A. G. Curto, J. Gómez Rivas, *ACS Photonics* **2020**, *7*, 1226.

[35] G. A. Ermolaev, D. V. Grudinin, Y. V. Stebunov, K. V. Voronin, V. G. Kravets, J. Duan, A. B. Mazitov, G. I. Tselikov, A. Bylinkin, D. I. Yakubovsky, S. M. Novikov, D. G. Baranov, A. Y. Nikitin, I. A. Kruglov, T. Shegai, P. Alonso-González, A. N. Grigorenko, A. V. Arsenin, K. S. Novoselov, V. S. Volkov, *Nat. Commun.* **2021**, *12*, 854.

[36] G. Mie, *Ann. Phys.* **1908**, *330*, 377.

[37] J. Roth, M. J. Dignam, *J. Opt. Soc. Am.* **1973**, *63*, 308.

[38] C. Tang, B. Auguié, E. C. Le Ru, *ACS Photonics* **2018**, *5*, 5002.

[39] X. Wu, S. K. Gray, M. Pelton, *Opt. Express* **2010**, *18*, 23633.

[40] J. A. Mason, G. Allen, V. A. Podolskiy, D. Wasserman, *IEEE Photonics Technol. Lett.* **2012**, *24*, 31.

[41] A. I. Kuznetsov, A. E. Miroshnichenko, M. L. Brongersma, Y. S. Kivshar, B. Luk'yanchuk, *Science* **2016**, *354*, aag2472.

[42] H. Sugimoto, M. Fujii, *Adv. Opt. Mater.* **2017**, *5*, 1700332.

[43] T. Hinamoto, S. Hotta, H. Sugimoto, M. Fujii, *Nano Lett.* **2020**, *20*, 7737.

[44] H. Sugimoto, T. Okazaki, M. Fujii, *Adv. Opt. Mater.* **2020**, *8*, 2000033.

[45] Y. Li, J. D. Cain, E. D. Hanson, A. A. Murthy, S. Hao, F. Shi, Q. Li, C. Wolverton, X. Chen, V. P. Dravid, *Nano Lett.* **2016**, *16*, 7696.

[46] J. G. DiStefano, A. A. Murthy, H. J. Jung, R. dos Reis, V. P. Dravid, *Appl. Phys. Lett.* **2021**, *118*, 223103.

[47] J. G. DiStefano, A. A. Murthy, S. Hao, R. d. Reis, C. Wolverton, V. P. Dravid, *Nanoscale* **2020**, *12*, 23897.

[48] M. Amani, M. L. Chin, A. L. Mazzoni, R. A. Burke, S. Najmaei, P. M. Ajayan, J. Lou, M. Dubey, *Appl. Phys. Lett.* **2014**, *104*, 203506.

[49] H. Sugimoto, T. Hinamoto, M. Fujii, *Adv. Opt. Mater.* **2019**, *7*, 1900591.

[50] T. Hinamoto, M. Hamada, H. Sugimoto, M. Fujii, *Adv. Opt. Mater.* **2021**, *9*, 2002192.

[51] U. Zywietz, M. K. Schmidt, A. B. Evlyukhin, C. Reinhardt, J. Aizpurua, B. N. Chichkov, *ACS Photonics* **2015**, *2*, 913.

[52] C. F. Bohren, D. R. Huffman, *Absorption and Scattering of Light by Small Particles*, John Wiley Sons Inc, New York **2008**.

[53] J. Mooney, P. Kambhampati, *J. Phys. Chem. Lett.* **2013**, *4*, 3316.

[54] E. D. Palik, *Handbook of Optical Constants of Solids II*, Academic Press, New York **2012**, 10.